

## The STIS CCD Spectroscopic Line Spread Functions<sup>1</sup>

T. Gull, D. Lindler,<sup>2</sup> D. Tennant,<sup>3</sup> C. Bowers, C. Grady,<sup>4</sup> R. S. Hill,<sup>5</sup> and E. Malumuth<sup>5</sup>  
*Laboratory for Astronomy and Solar Physics, Code 681, NASA's Goddard Space Flight  
Center, Greenbelt, MD, 20771*

**Abstract.** We characterize the spectroscopic line spread functions of the CCD modes for high contrast objects. Our goal is to develop tools that accurately extract spectroscopic information of faint, point or extended sources in the vicinity of bright, point sources at separations approaching the realizable angular limits of *HST* with STIS. Diffracted and scattered light due to the *HST* optics, and scattered light effects within the STIS are addressed. Filter fringing, CCD fringing, window reflections, and scattering within the detector and other effects are noted. We have obtained spectra of several reference stars, used for flux calibration or for coronagraphic standards, that have spectral distributions ranging from very red to very blue. Spectra of each star were recorded with the star in the aperture and with the star blocked by either the F1 or F2 fiducial. Plots of the detected starlight along the spatial axis of the aperture are provided for four stars. With the star in the aperture, the line spread function is quite noticeable. Placing the star behind one of the fiducials cuts the scattered light and the diffracted light is detectable even out to 10000 Å. When the star is placed behind either fiducial, the scattered and diffracted light components, at three arcseconds displacement from the star, are below  $10^{-6}$  the peak of the star at wavelengths below 6000 Å; at the same angular distance, scattered light does contaminate the background longward of 6000 Å up to a level of  $10^{-5}$ .

### 1. Introduction

The distinctive advantages of *Hubble Space Telescope (HST)* are near-diffraction-limited imaging performance and access to the ultraviolet. The Space Telescope Imaging Spectrograph (STIS) takes advantage of the near-diffraction-limited capability of *HST* and provides spectral dispersions ranging from  $R \simeq 500$  and 10,000 from 1175–10,000 Å and  $\simeq 30,000$  to 180,000 from 1175 to 3200 Å. The optical design and detector performance of STIS was carefully matched to science problems that the STIS Instrument Development Team (IDT) realized could be addressed with high angular resolution and selected spectral dispersions. We designed the detector formats to utilize the angular resolution of the primary optics. For the CCD modes (1650–10,000 Å,  $R \simeq 500$  and 10,000), the pixel sampling is  $0''.0504$ . In keeping with the philosophy of developing the second generation of instruments for *HST*, state-of-the-art detector technology was pushed to obtain the best detectors possible for space observations and numerous spectral modes were installed to provide a range of

---

<sup>1</sup>Based upon observations with the NASA/ESA *Hubble Space Telescope*, obtained at the Space Telescope Science Institute, which is operated by the Association of Universities for Research in Astronomy, Inc., under NASA contract, NAS 5-26555.

<sup>2</sup>Advanced Computer Concepts

<sup>3</sup>Naval Academy

<sup>4</sup>National Optical Astronomy Observatory

<sup>5</sup>Science Systems Applications, Inc.

resolving powers. Late in testing of the CCD modes, we realized that increased transparency in the near red of the silicon bulk material led to increased internal scatter within the detector and support substrate. This red scatter would complicate spectroscopy, direct imagery and especially coronagraphic imagery done with the STIS CCD.

Success of STIS is measurable in many ways. With each cycle of competition for *HST* observational time, many successful proposals use the STIS. Already, key discoveries include measurements of black hole masses in the nuclei of many galaxies, and the cores of globular clusters, of the spectroscopic transit of a planet across the surface of a distant star, of the lack of planets in globular clusters, of measurements of the Gunn-Peterson effect and of the Lyman alpha forests, of the first ultraviolet spectra of gamma ray bursters, and of nebular structures in very close vicinity to bright stars. The *HST/STIS* has broken many barriers to ground-based spectroscopy, yet data reduction and analysis continues to be challenging when we attempt to pull out weak, extended structures close to a bright central source. As we have learned more and more about the performance of STIS, we have felt encouraged to push the limits of its capabilities. In this discussion, we present some measures of the line spread function for the CCD spectroscopic modes as a function of wavelength. In the future, we hope that software will be developed to enable all users to take full advantage of the remarkable rejection that STIS provides off axis. More importantly, we hope that this information on the realized performance of STIS will provide insights for improved instrument performance of future ground-based and especially space-based instruments.

For the *HST/STIS* user, many observations can be accomplished routinely. If two objects are at the classical separation (one full at half maximum separation), then the data reduction/analysis is relatively straightforward. Here we address optical performance that must be taken into account when the relative intensities are  $> 20$ . With the potential of reaching statistical  $S/N > 20$ , large contrast factors can be addressed. In short this discussion is in the very important application when a very low extended source, or even a faint point source, is detectable near a significantly brighter, point source.

## 2. Examples of a STIS CCD High Contrast Observations

We start with a spectrum of a K0 star (HD 181204) dispersed by the G750L grating from 5000 to 10,000 Å (Figure 1). The top and middle spectra display the same spectrum with relative flux scales of 100. The bottom spectrum is of the same star behind the F1 (0'5) fiducial<sup>1</sup> which blocks the core light by nearly four orders of magnitude. The grey scale for the bottom spectrum is 1/300th that of the top spectrum. Longward of 7000 Å, the silicon structure of the CCD absorbs less radiation, and the light is reflected within the chip structures. Diffuse scattering becomes increasingly apparent with wavelength and spreads across the CCD. The CCD in the near-red behaves much like a Fabry-Perot interferometer, and develops wavelength-dependent fringes in response to the dispersed light. Properly executed flat fields can be used to correct the fringed response for objects positioned within the aperture. Recently, Malumuth et al. (2002) developed a calibration scheme for objective grating spectra of objects in the STIS CCD parallel modes (see also Malumuth et al. 2003). The fringes seen in the bottom image of Figure 1 are not CCD-induced fringes, but the classical fringes due to diffraction of the telescope optics. In a perfect spectrograph, these fringes would be the limiting factor in observing faint sources in the vicinity.

The collapsed Line Spread Function (LSF) is plotted in Figure 2 for the same spectra in Figure 1. The upper trace is of the unobstructed star LSF sampled through the  $52'' \times 0'.2$  aperture.

---

<sup>1</sup>The STIS has an aperture wheel that allows for a selection of optimized apertures to fit the desired scientific observation. An internal calibration system (WAVECAL) feeds light from a Pt(Cr) lamp to provide reference wavelengths for wavelength and velocity measures. Positional information is defined by two fiducials (F1, which is 0'.5 wide, and F2, which is 0'.8 wide) on each long aperture. The aperture wheel encoding permits very precise placement of the apertures, sufficiently accurate in position, that a stellar image can be blocked by rotating the aperture into position. The fiducial tests in this paper were performed with the  $52'' \times 0'.2$  and the  $52'' \times 0'.1$  apertures.

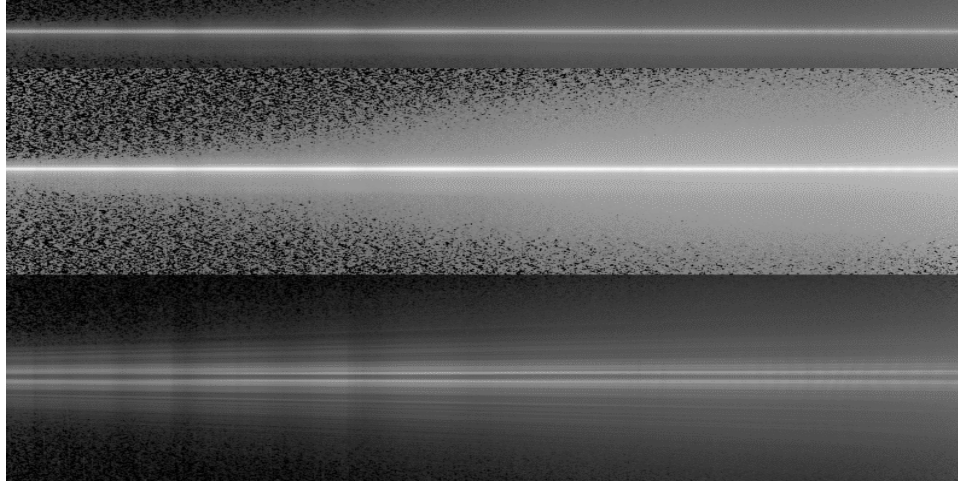


Figure 1. Spectra of HD 181204 (MIII) from 5000 to 10,000 Å through the  $52'' \times 0.2''$  STIS aperture. The top and middle spectra are the same spectrum, but with a grey scale change of  $10^2$ . The bottom spectrum is with the star placed behind the F1 fiducial ( $0.5''$  wide), displayed with a grey scale  $1/300$ th that of the top spectrum. The *HST* diffracted light pattern is now visible.

The middle trace is of the same star, HD 181204, placed behind the F1 fiducial ( $0.5''$  wide) and the bottom trace is with the star placed behind the F2 fiducial ( $0.8''$  wide). The fiducial cuts the wings of the LSF by  $10^2$ . We note that this spectral LSF is a linear approximation of a much more complex function. In the stellar spectrum spread horizontally across the two-dimensional CCD, each wavelength has a scattering function that spreads in two dimensions. The narrow aperture at the entrance to the STIS cuts the PSF of *HST* to a thin slice that is then modified by each optical element. In the ideal situation, this modification would simply be the spectral separation of the input light. However each optical element can contribute scatter or modulation to the light, creating a PSF response that is wavelength dependent. We find that the major effect is light scattering in the CCD detector itself and that the scattering becomes more pronounced to the red part of the spectrum. However to get reasonable S/N measures of the LSF, we had to collapse the data in the spectral direction to measure the LSF along the cross-dispersion, the angular or the spatial direction. The reader is cautioned that a wavelength LSF is needed, especially at wavelengths longward of 7000 Å. Between 3000 and 7000 Å, an averaged LSF, scaled with wavelength due to *HST* optics diffraction effects likely will suffice.

Scattered light is a major problem for faint, extended or complex structures along the aperture. Eta Carinae, with the Homunculus (a bi-lobed nebula plus disk system of ejecta) is one such complex structure with scales well matched to the angular resolution of *HST*. Most of the nebula is a reflection nebula shell with some ionized metals, but neutral hydrogen. Close to the star is a series of emission structures, including a Little Homunculus (Ishibashi, et al. 2002). Figure 3 shows an extracted portion of three spectra including Balmer alpha (G750M, centered on 6768Å). Eta Carinae is centered within the  $52'' \times 0.1''$  aperture in the lower spectrum. In the logarithmic stretch across five decades, a faint ghost is noticeable to the lower right of the bright, broadened Balmer alpha emission profile of the star. Faint nebular emission consisting of narrow Balmer alpha and [N II], [S II] emission lines can be seen, but the brightness is only slightly above the video pickup, with  $\simeq 4DN$  amplitude. The middle and top spectra were recorded with the  $52'' \times 0.2''$  aperture, but with the F2 ( $0.8''$  width) fiducial rotated to block the star. The middle spectrum (10 seconds CR-SPLIT) brings out the nebular emission lines well above the video pickup, and the scattered starlight continuum can be seen, including the broad Balmer alpha emission, complete with a nebular absorption line. Some video pickup is noticeable. The top spectrum (150 seconds CR-SPLIT) goes very deep, but

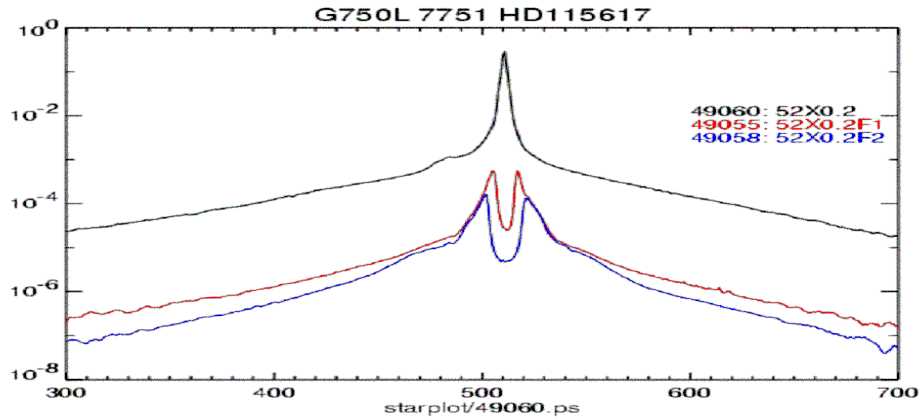


Figure 2. Collapsed Line Spread Function (LSF) for G750L (5000 to 10,000 Å) of the HD 181204 (MIII) (Figure 1). The upper trace is the LSF for the unobstructed spectrum. The middle trace is the LSF for the star placed behind the F1 (0.5 wide). The bottom curve is the LSF for the star placed behind the F2 (0.8 wide).

some of the scattered Balmer alpha emission has saturated at the edge of the fiducial and is bleeding into the nebular portion of the spectrum. Closer inspection of this spectrum pulls out over twenty unique narrow nebular emission lines, two of which are [Sr II] detected for the first time (Zethson, et al. 2000).

### 3. Known Limitations

As with any spectrograph, each optical element alters the output. Some changes are not desirable, whether they are diffraction effects, scattered light, faint reflections at every transmitting surface, stray light, or detector performance. The challenge is to anticipate these problems and to minimize deleterious effects on the product. STIS is no exception, and as shown in this paper, we are pushing the instrument capabilities to the realizable limits. Indeed one major reason for preparing this paper is to document the realized instrument capabilities and to sensitize designers of future spectrographs to shortcomings that must be overcome if astronomers wish to study complex systems with even higher contrasts.

Each first order grating has a blocking filter to ensure no second order (blue) leakage contaminates first order spectra at the red end. Each blocking filter is attached directly to the grating mount. Collimated light passes through these filters both in the incident and diffracted beam. A small modulation is detectable especially in the spectra of calibration emission lamps where the  $f$ /ratio of the optical system is very large and the intrinsic line widths are much narrower than the resolving power of the spectrograph ( $R \simeq 500\text{--}10,000$ ). For astronomical continuum sources the modulation is significantly less than a percent and for emission line sources, the modulation would be a few percent for intrinsic linewidths approximately  $20 \text{ km s}^{-1}$ . Spectroscopy of NGC 7009 yielded a measured peak-to-peak modulation of 3% for the ratio of [O III] 5007 Å/4959 Å (Rubin et al. 2001).

The ghost image (Figure 3) is of much greater concern. Direct images (Figure 4) show a faint double ring to one side of each bright star image. The position of these rings moves relative to the star image. R. S. Hill (63 and 65) analyzed many direct and spectroscopic images recorded by STIS (Figures 4, 6 and 7). The integrated flux of the double ring is a few percent of the total flux of the star. Figure 8 shows the path traced by the principal ray impinging upon the CCD. The CCD surface reflects the focused image, at  $f/48$ , back to the fused silica housing window (necessary to prevent contamination accumulating on the CCD surface!). Reflections from both window surfaces

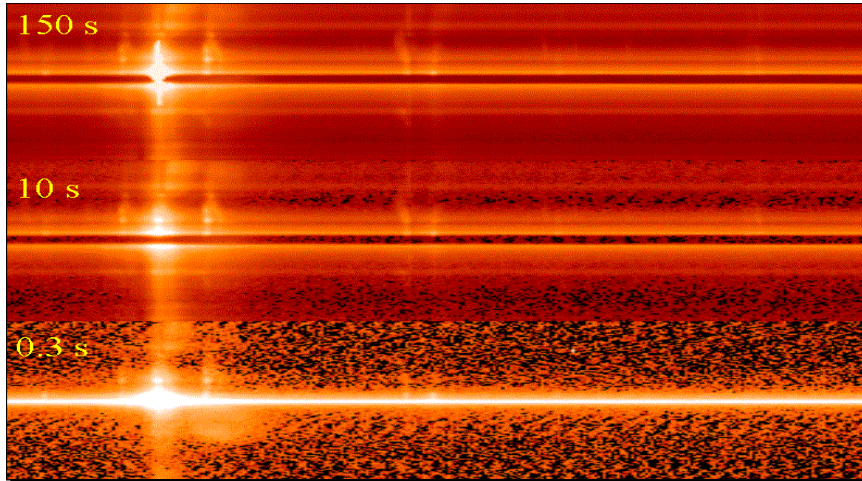


Figure 3. Spectra of Eta Car and Very Nearby Ejecta from 6400 to 7000 Å, plotted with a dynamic log scale of  $10^5$ . Bottom: Eta Carina in the  $52'' \times 0.1''$  aperture (exposure 0.3 s). The broad, diffuse structure to the right and just below the Balmer alpha P-Cygni emission line is a ghost image due to reflections off the CCD detector window. Middle: Eta Car behind the F2 ( $0.8''$ ) fiducial (10 second CR-SPLIT). Top: 150 second, CR-SPLIT=2 exposure. The stellar Balmer alpha spills over the fiducial into the extended nebula. Each spectrum extends  $-2''$  to  $+2''$  from Eta Car. The ghost, seen when the star is within the aperture, is greatly decreased by the fiducials as the scattered light is suppressed.

result in the two out of focus, displaced images next to each star in Figure 4. Hill's report (2000) demonstrates that the rings on direct images are well behaved. Lines, extending through each stellar and associated pair of ghost images, come to a common region on the detector. Figure 5 reproduces his measures of the positional displacements. The dispersed spectrum of a star, shown in Figure 6, demonstrates that the double rings build up a shoulder offset below the stellar spectrum. The integrated amplitude, which changes with wavelength, is a few percent of the total stellar flux in the red, but nearly negligible in the 2000–3000 Å spectral region as an antireflection coating was placed on the window for the blue portion of the spectrum.

Quite a different response is noted for WAVECAL spectra (Figure 7). The double ring phenomenon is not present, but a series of fringes in the approximate positions, expected for the CCD window ghosts, are seen. A spectrum of the brightest portion of the Orion nebula was recorded of H alpha and [N II] lines. No fringes were observed at the ghost positions. Twelve sub-exposures were combined by CALSTIS using a cosmic-ray rejection algorithm. Detection of the ghost is marginal as the relative brightness per pixel is  $\simeq 10^{-4}$  that of the peak emission line brightness. However, WAVECAL exposures provide fringe amplitudes  $\simeq 10^{-3}$  of the peak emission line brightnesses. We realized that WAVECALs were done through a different, highly collimated, optical train, before the STIS aperture.

Lifetime of a mechanism in a space instrument is always a concern. The STIS shutter moves in and out of the input light path to prevent light contamination by STIS of any other instrument operating in parallel. The backside of the shutter has a mirror that feeds light into the instrument for LAMP calibrations. To minimize the movement of the shutter, an alternate light path feeds light from the calibration optical train through a permanently mounted mirror and a hole in the second relay mirror (the relay mirrors correct for optical aberrations of *HST*), and to illuminate the STIS aperture. This mode, labeled HITM (hole in the mirror ... what else!), is within the shadow of the *HST* secondary. Thus the HITM mode feeds light with a very large f/ratio beam into STIS. The lamp intrinsic line widths are far narrower than the spectral resolving power of the first order

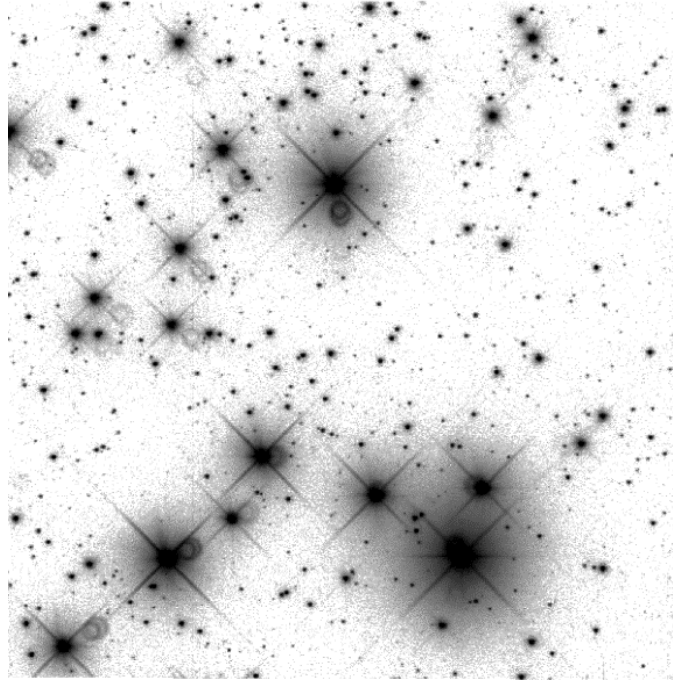


Figure 4. Broad-Band Direct Image Recorded by the STIS CCD. Each stellar image has two ghost rings due to reflections off of the CCD detector housing window. Note that the reflections relative to the stellar position move about a point due to the pupil plane being a significant distance behind the detector.

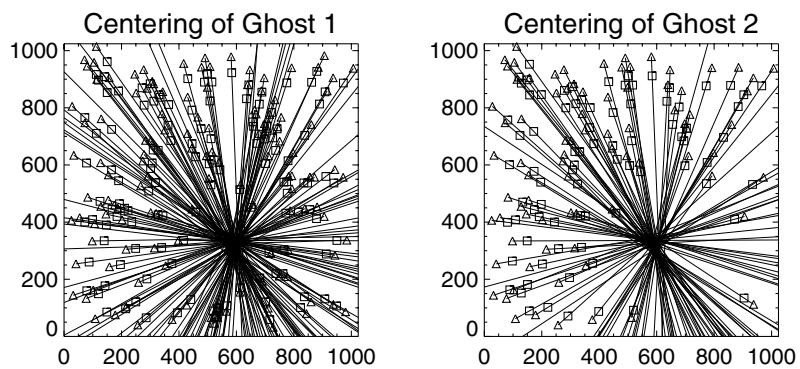


Figure 5. Centering of the Two Ghosts within the CCD Detector Format. A line, drawn through the stellar image and the centers of one of the ghosts, extends to a common region on the CCD format. With the spectrum dispersed across in row 511, the ghost is BELOW the spectrum. Were the spectrum placed in row 100, the ghost would appear ABOVE the spectrum.

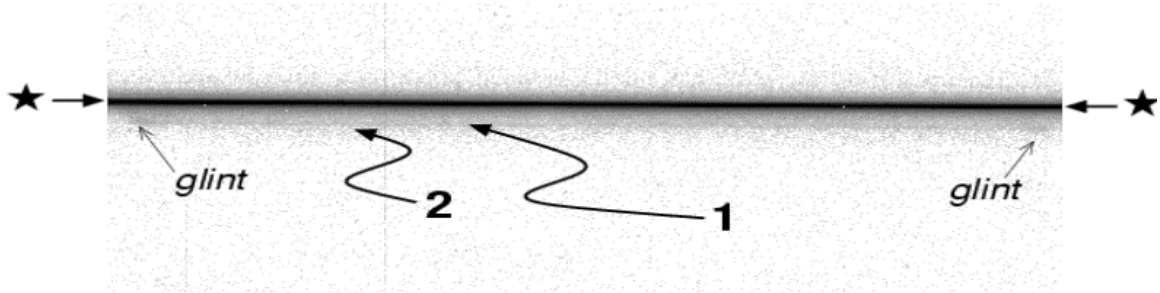


Figure 6. Stellar Spectrum with the Ghost. The ghost flux is a few percent of the stellar flux, but extends over a number of pixels. Typical amplitudes per pixel are a few parts in  $10^4$  of the peak stellar amplitude.

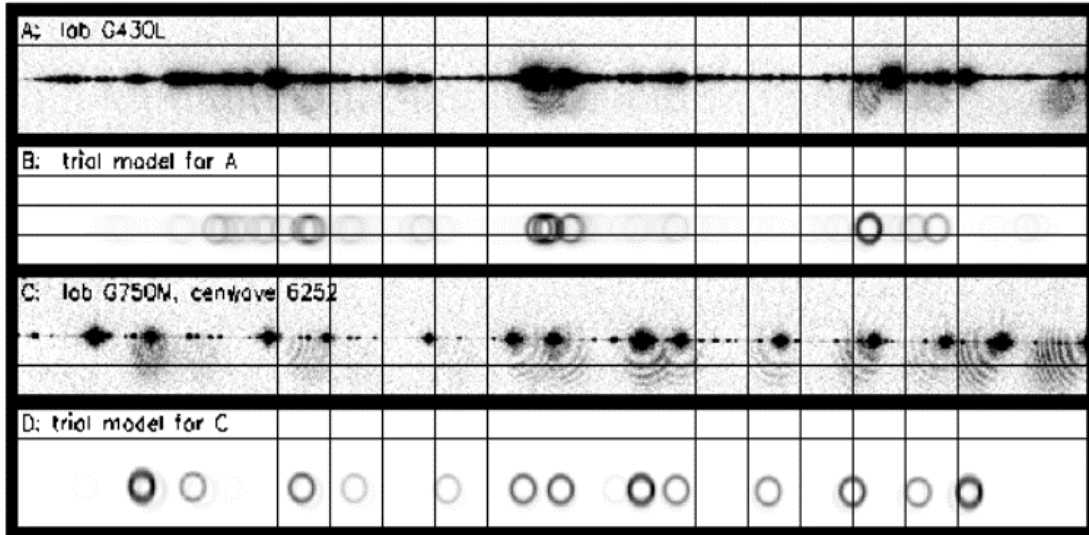


Figure 7. Sample Calibration Spectra and Simulations. Prelaunch external and internal lamp spectra demonstrate that the ghost position shifts with respect to the line position along the dispersion and that the HITM ghosts are fringed. The HITM optical beam is nearly collimated relative to the HST  $f/24$  optical beam.

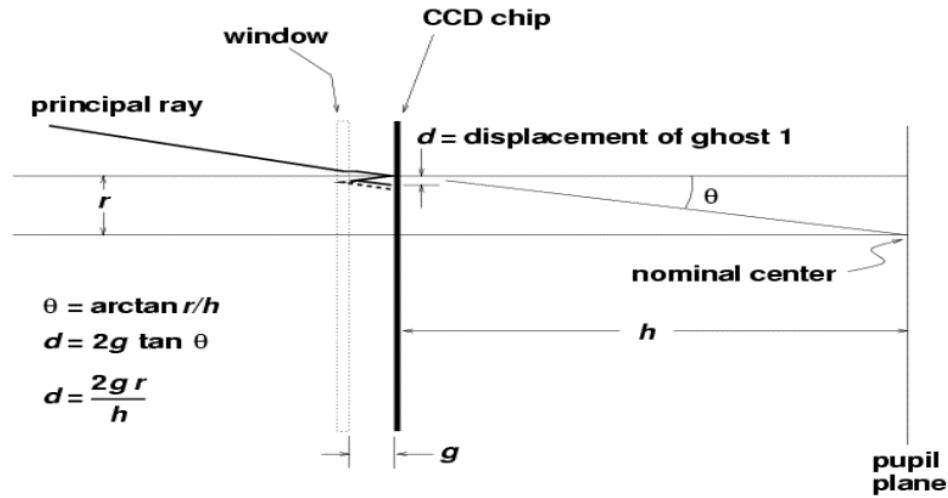


Figure 8. Optical Paths of the Incident Light and the Reflected Light. The ghost images are displaced from the primary spot due to the pupil plane being at a significant distance behind the detector surface.

gratings. The CCD-reflected light is reflected back by the two surfaces of the detector window and is modulated. We do not detect modulation of continuum sources, internal or external, because the wavelength variation is continuous. Hence we see rings instead of fringes. We confirmed this by a comparison of a LAMP spectrum to a HITM spectrum. The LAMP mode overfills the  $f/24$  beam of the STIS collimator. The LAMP spectrum for the Pt(Cr) lamp is noticeably less than the HITM spectrum. As nearly all astronomical sources have intrinsic line widths (thermal, turbulence, etc.), the fringing is negligible.

#### 4. Spectroscopic LSF Observations

To characterize the faint scattering characteristics of STIS, spectroscopic LSF measurements were done of stars placed within a long aperture and then blocked by a fiducial. Indeed, we realized that characterization of coronagraphic imagery (see Grady, et al. 2003) could be enhanced by these spectroscopic measurements. The *HST* point spread function for a star is a weighted function of the spectral distribution. For a well-behaved panchromatic detector, the *HST*/STIS response would be expected to be spectral distribution of a known star weighted by the diffraction-limited *HST* PSF and sampled by the selected STIS entrance aperture. However, the STIS CCD has a very significant scattering component longward of  $7000 \text{ \AA}$  as demonstrated in Figures 1 and 3. Our desire to quantify the detector scattering component and to understand the effects on observations led to requesting stellar measurements performed with proposal 8844.

Four stars, point-like with respect to *HST*'s angular resolving power, were selected. Other criteria included no measurable infrared excess (suggesting possible dust and gas surrounding the star); reasonable exposure times to record the scattered light passed by the STIS aperture fiducials F1 ( $0''.5$ ) and F2 ( $0''.8$ ); not be in a crowded field; and good accessibility, namely close to the orbital pole. STIS has an aperture wheel and a grating wheel. The selected aperture and grating are rotated into the light path. Internal calibration spectra are required to determine the spectral position on the detector. A WAVECAL is recorded along with each astronomical observation. In line identifications of the Weigelt blob B and D, located close to Eta Carinae, Zethson (2000) found that the measured, velocity-corrected wavelengths were accurate to about one-fifth of a STIS CCD pixel, based upon measured versus laboratory wavelengths of about 2000 emission lines. Position along any long

aperture is referenced by two fiducials within each aperture. As the aperture wheel is very finely encoded, the F1 or the F2 fiducial can be precisely placed in front of the stellar image. Currently only F2 for the  $52'' \times 0''.2$  aperture is supported for routine observations. However other fiducials have been used. In proposal 8844, we used the F1 and F2 fiducials for both the  $52'' \times 0''.2$  and the  $52'' \times 0''.1$  apertures with excellent success.

The most pressing criterion was to accomplish these observations in a reasonable number of orbits. We chose to use all three low dispersion gratings: G750L (5000 to 10,000 Å), G430L (3000 to 5000 Å) and G230LB (1600 to 3100 Å). As there are approximately forty primary settings for the M gratings, only the most frequently used M-mode settings were tested: G750M (8561 Å and 6768 Å), G430M (4961 Å and 3936 Å) and G230MB (2836 Å). Most grating settings were used with the A0V star, HD 141653, as the exposure times were reasonable and much could be learned throughout the spectrum. Only a subset of grating settings were used in the blue for the BD+75D325 (WD) and in the red for HD 115617 (GV) and HD 181204(MIII). The observed combinations are listed in Table 1. The WD, BD+75D325, was selected because it is a primary standard used in monitoring the sensitivity of STIS. The other three stars were selected because they had proved to be excellent reference stars for STIS coronagraphic observations (Grady, 2003) and because they spanned the spectral types from MIII to GV to A0V. Initially, we thought that the reference PSF of stars of intermediate spectral types could be modelled by a weighted combination of the PSF's measured for these stars. However, the best reference PSF's are those of similar stars taken during orbits immediately before or after the stars of interest because thermally induced collimation and focus changes are of greater impact.

Table 1. Stars Observed in Proposal 8844 for this Study

Star	SpT	APER	G750L	G750M	G430L	G430M	G230LB	G230MB
BD+75D325	WD	$52 \times 0.2$	–	–	A,F1,F2	A,F1 4961	A,F1,F2	A 2836
HD141653	A0V	$52 \times 0.2$	A,F1,F2	A,F1 6768	A,F1,F2	–	A,F1,F2	–
"	"	$52 \times 0.2$	–	A,F1,F2 8561	–	A,F1,F2 3936	–	–
"	"	$52 \times 0.1$	–	A,F1,F2 8561	–	A,F1,F2 4961	–	–
HD115617	GV	$52 \times 0.2$	A,F1,F2	A,F1,F2 6768	A,F1,F2	–	A,F1,F2	–
HD181204	MIII	$52 \times 0.2$	A,F1,F2	A,F1,F2 6768	A,F1,F2	–	A	–

<sup>a</sup>For GXXXXL(B) grating tests, the grating settings are the default central wavelengths. For GXXXXM(B) the grating settings are listed as the central wavelength in Å. A = star in slit. F1 = star behind fiducial F1 (0.5/arcsec). F2 = star behind fiducial F2 (0.8/arcsec).

Exposure times, which are not listed, were selected to keep the recorded spectra significantly below the 32,000 DN levels with the CCD GAIN = 4. Where the fluxes were significantly lower, GAIN = 1 was used to keep above video pickup levels close to the star. As the desired dynamic range is quite large, we rapidly reach flux levels affected by detector noise, cosmic ray events and even bias shifts across the CCD columns. Indeed some LSF plots exhibit a pronounced asymmetry from below the star in the spatial direction to above the star. This is a known bias shift problem. Correcting for it is not a simple matter. We chose to not correct for the shift as a means of cautioning the observer that it is there.

The line spread functions are presented in Figures 2, 9–13. These are averaged LSFs. Each spectrum is precisely aligned using WAVECAL lamp spectra and the trace of the stellar spectrum, or the illuminated edges of the fiducial, when the star is blocked by the fiducial, F1 or F2. We caution the reader that these LSFs are collapsed along the spectral dispersion (re-sampled row) direction. For the G750L spectra, the average is taken from 5000 Å to 10,000 Å, and is heavily weighted by scatter beyond 7000 Å. For contrasts up to  $10^3$ , the current data is sufficient, but a wavelength-dependent LSF from 5000 to 10,000 Å will have to be modelled as the measurements do not have sufficient S/N for complete measure. For Figure 2 and 9–13, the flux along the spatial (cross-dispersion) axis is logarithmic ranging from  $10^0$  to  $10^{-8}$ . Each CCD pixel subtends  $0.0504''$ .

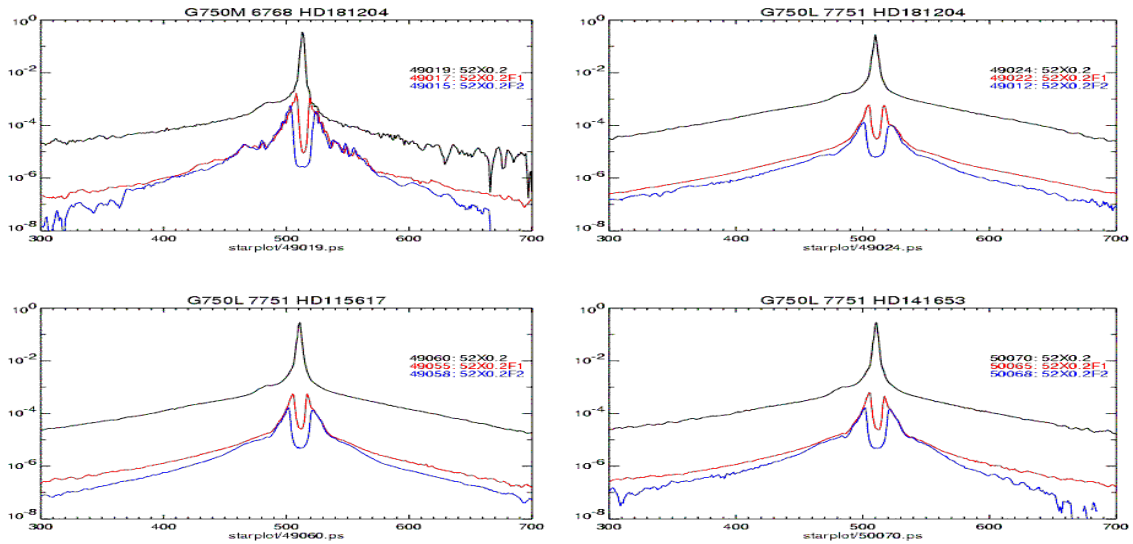


Figure 9. Comparison of LSF for G750L for HD 181204 (MIII, upper right), HD 115617 (GV, lower left), and HD 141653 (A0, lower right). Upper left is the LSF for G750M for HD 181204 (MIII) centered at 6768 Å.

These plots extend from approximately  $10''$  below to  $10''$  above the star, which is centered near row 512.

The top trace is of the star centered in the  $52'' \times 0.2$  aperture and is normalized to the total measured flux. The LSF drops slowly, but relatively symmetrically. At  $10''$  distance from the star, the detected flux is  $\sim 10^{-4}$  of the total flux. The central trace is the LSF with the star placed behind F1. The flux at the position of the star drops by  $10^4$ , and the off-axis scattered light drops by a factor of  $10^2$ . The bottom trace is the LSF with the star placed behind F2. The scattered light is not affected significantly in the innermost few arcseconds, but at  $\sim 10''$ , the scattered light is decreased by a factor of two compared to the scattered light from the F1 fiducial measurement.

The left-hand shoulder is the ghost that we discussed above (Figures 3–6). Placing the star behind either fiducial drops this shoulder as expected. However, the light that passes the fiducial, diffracted and scattered light from the telescope, also produces ghosts. As the signal/noise is excellent, we can see the fainter ghost due to the left edge of the fiducial for F1 and even for F2. The ghost for the right hand portion of the light passing the fiducial contributes to filling in the area subtended by the fiducial and to the flux on the left hand side of the fiducial. If the star were in row 100, the ghost would shift above the spectrum.

In the following section, we will intercompare LSFs for different grating combinations with spectral type. The top curve is always the star in aperture; the middle curve is F1; and the bottom curve is F2. These fiducials were moved in and out without re-centering the star between observations. As demonstrated by the symmetry of the stellar core and the scattered light on both sides of the fiducials, the relative offsets are excellent. Indeed, success of proposal 8844 is good evidence to extend support to all four fiducials.

## 5. LSF Intercomparisons

The LSFs (Figure 9) for the three coronagraphic reference stars are collapsed from 5000 to 10,000 Å. They vary because of the CCD response to the very different stellar spectral distributions. The AOV star LSF (lower right) drops off faster due to the blue spectral distribution. Indeed, this LSF,

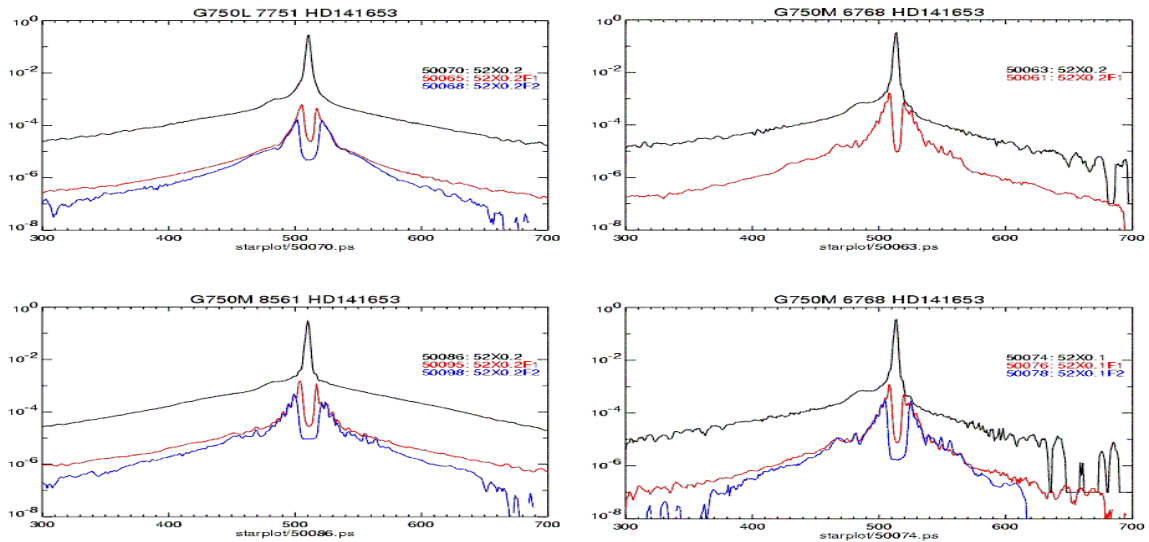


Figure 10. Comparison of LSFs for HD 114653 (GV) Upper left: G750L Lower left: G750M (8561 Å) Upper right: G750M (6768 Å) with  $52'' \times 0.2''$  aperture. Lower right: G750M (6768 Å) with  $52'' \times 0.1''$  aperture.

weighted towards 5000 Å relative to 10,000 Å, is similar to the spectral LSF measured by the G750M grating (upper left) centered at 6768 Å.

Figure 10 compares LSFs for HD 114653 (A0V) for G750L and selected G750M settings. The G750M (8561 Å) LSF (lower left) is very similar to the G750L LSF (upper left). The G750M (6768 Å) LSF (upper right) wings drop off faster for the F1 fiducial than the LSF centered on 8561 Å. The G750M (6768 Å) grating setting was observed with both apertures. Little difference, other than S/N, was noted.

The G430L LSFs for all four stars are plotted in Figure 11. As expected, scattering drops off faster than for the G750L LSFs, since the telescope optics diffraction pattern is sharper and the CCD silicon layer is optically much thicker. Visible-wavelength photons do not penetrate very deep into the silicon layer. By contrast, the CCD is nearly transparent to photons near 10,000 Å and the diffraction pattern is twice as large. The G430M LSFs produced by the four stars are quite similar: the diffraction pattern is close to the core of the star; the ghost is easily seen on the left shoulder. Knowledge of the bias level is now a significant problem as demonstrated by the asymmetry of scatter above and below the star.

Figure 12 plots three measures of the G430M LSF in comparison to the G430L LSF. S/N is an issue as scattered/diffracted flux drops down to levels marginally detectable with 32000 DN encoding range. Determining the bias level is also a problem. BD+75D325 LSF measures are strongly limited by detector background. The ghost signal appears stronger for the G430M (4961 Å) setting than for the 3936 Å setting due to the antireflection coating applied to the window for the blue optimization.

While several LSFs were measured for the G230LB and G230MB gratings, they differed only in S/N. Figure 13 shows the best LSF measures for BD+75D325. The ghost on the shoulder is significantly weaker than for spectra to the red. Scatter measurements in all three LSFs are limited by the finite DN range integration time. The three LSFs match so well that we are tempted to combine all three. The fiducials in the G230LB and G230MB modes primarily attenuate the core of the telescope PSF. The STIS CCD does not contribute a significant scatter component as the blue photons are absorbed at the surface of the silicon.

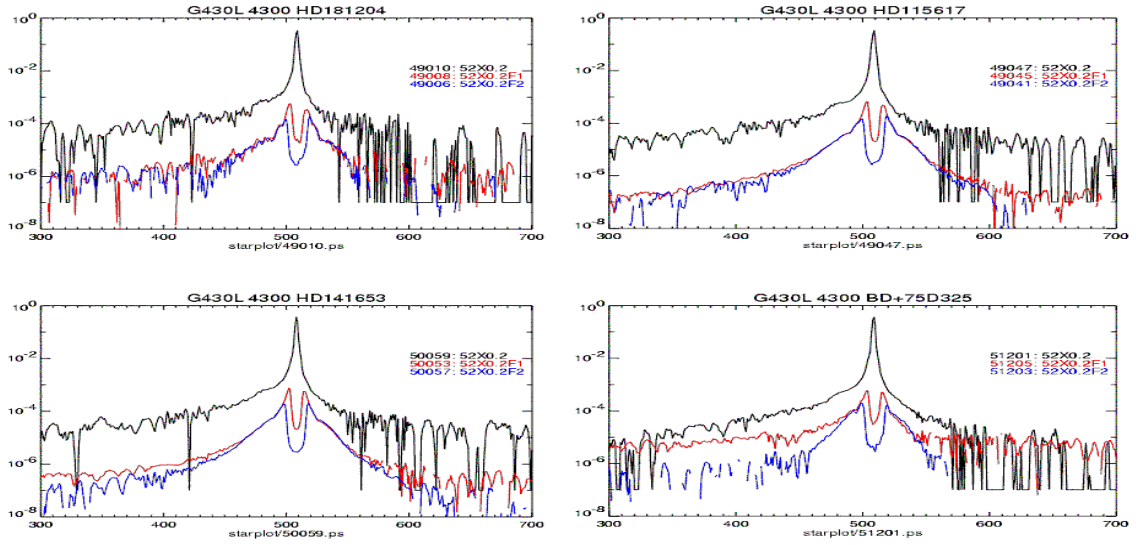


Figure 11. G430L comparisons for all four stars.

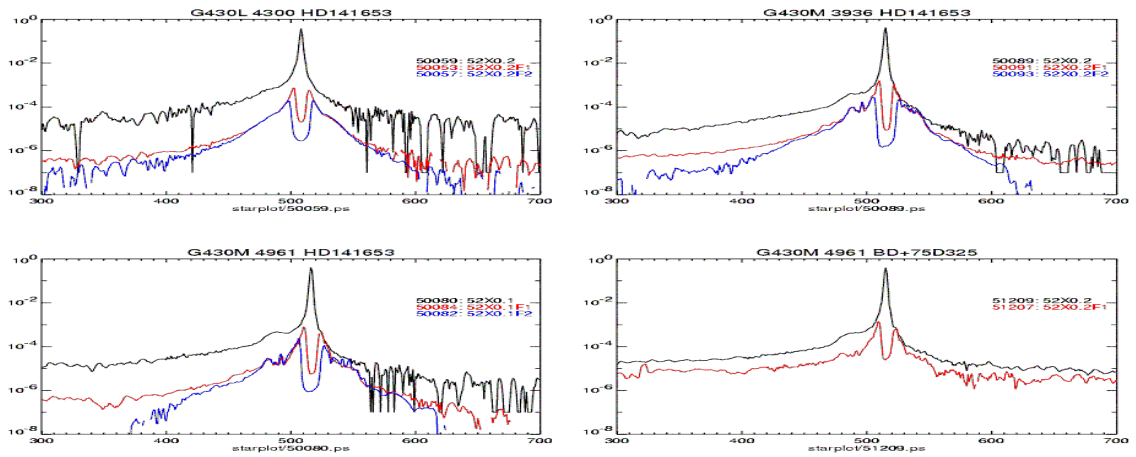


Figure 12. G430L and G430M comparisons for A0V HD141653 and WD BD75+325.

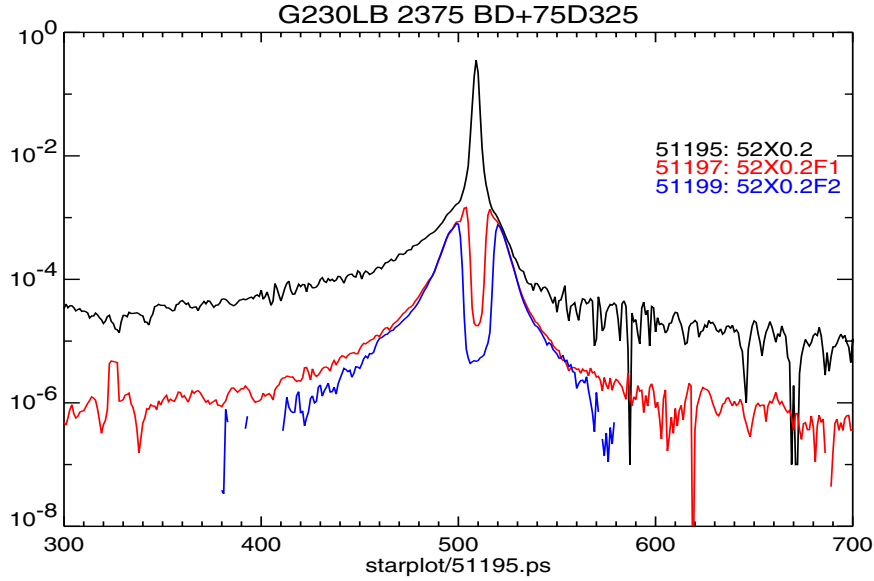


Figure 13. G230L LSF comparisons for WD BD75+325.

Figure 14 brings together the contribution to the background as a function of wavelength for an angular displacement offset by three arcseconds from the star in the  $+Y$ -direction. The three curves are for the star in the aperture, behind the F1 fiducial and then behind the F2 fiducial. Compared to the total normalized flux, the scattered/diffracted starlight contribution is below a few parts in  $10^5$  from 2000 to 6000 Å. Longward of 6000 Å the scattered light component becomes noticeable, primarily due to scatter in the STIS CCD. It climbs to a level of  $\sim 10^{-3}$  at 10,000 Å. With the star placed behind either fiducial, the scattered component drops 100-fold at 10,000 Å and is below  $10^{-6}$  shortward of 7000 Å. The rise in scattered light shortward of 3000 Å is consistent with measured *HST* light scatter due to roughness of the mirror surface. Finally we wish to point out that the LSF measures in this discussion are really a linear approximation to a scattering phenomenon that must radially transmit through the CCD chip in a fairly random pattern. This pattern will depend on the details of the CCD fabrication: how thick and uniform is each layer of etched circuitry and the uniformity of sensitivity. From Malumuth et al. (2002) we learned that the CCD chip is wedge-shaped and that the sensitivity fringes are distorted by this apparent shape. A proper model of the detected scattered light would also have to take into account the smoked support glass that supports the CCD chip within the housing, necessary to help the CCD survive during the launch vibrations.

## 6. Conclusions

This discussion describes the instrumental scatter of STIS in combination with *HST*. We observed four stars ranging from a WD to MIII in spectral type, working in coordination with coronagraphic observers. Future work is intended to define a tool for subtracting the ghost feature, and possibly defining a wavelength-dependent LSF.

**Acknowledgments.** We are grateful to the Space Telescope Science Institute STIS Team, their contribution of observing time and positive encouragement in reducing and interpreting the data. One of us (Don Tennant), as a volunteer summer student from the United States Naval Academy, provided much of the data reduction used in this paper. Mr. Keith Feggans assisted in preparation of the figures for this publication.

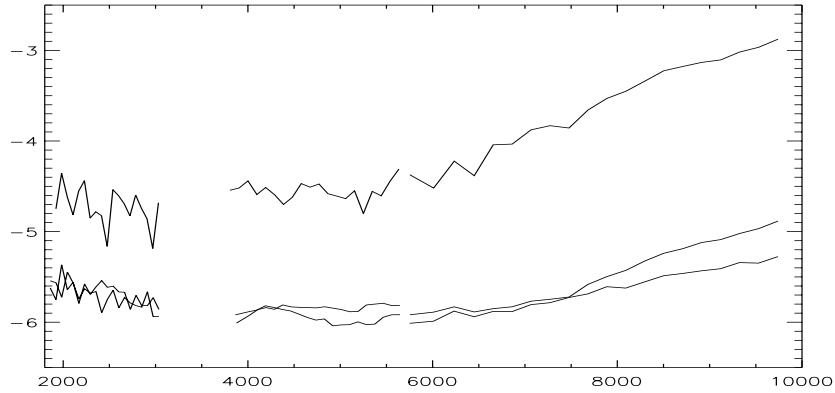


Figure 14. The Measured Scattered Light Component as a Function of Wavelength at a Position Offset  $3''$  from the Star in the cross dispersion direction on the CCD. Abscissa:  $\text{alog}_{10}(\text{flux})$  relative to the total flux. Top curve: scattered light with the star centered within the STIS  $52'' \times 0''.2$  aperture; bottom curves: measures of the scattered flux with the star is positioned behind F1 or F2.

## References

- Grady, C. A. 2003, this volume, ??
- Hill, R. S. 2000–2001, *STIS Postlaunch Quick Look Reports*, No. 63 and 65  
[http://hires.gsfc.nasa.gov/stis/postcal/quick\\_reports./quick\\_reports.html](http://hires.gsfc.nasa.gov/stis/postcal/quick_reports./quick_reports.html)
- Ishibashi, K., et al. 2002, *AJ*, submitted
- Malumuth, E., et al. 2002, *PASP*, accepted
- Malumuth, E., et al. 2003, this volume, ??
- Rubin, R., et al. 2001, *MNRAS*, 334, 777
- Zethson, T. 2000, PhD. Dissertation, Lund University, Sweden
- Zethson, T., Gull, T., et al. 2000 *AJ*, 12, 34